Mach Reflection and Expansion of Two-Dimensional Dispersive Shock Waves

Gino Biondini,[1,2] Alexander Bivolcic,[1] and Mark A. Hoefer[3]
[1]Department of Mathematics, State University of New York, Buffalo, New York, USA
[2]Department of Physics, State University of New York, Buffalo, New York, USA
[3]Department of Applied Mathematics, University of Colorado, Boulder, Colorado, USA

(Received 1 November 2024; revised 28 April 2025; accepted 2 July 2025; published 5 August 2025)

The oblique collisions and dynamical interference patterns of two-dimensional dispersive shock waves are studied numerically and analytically via the temporal dynamics induced by wedge-shaped initial conditions for the Kadomtsev-Petviashvili II equation. Various asymptotic wave patterns are identified, classified, and characterized in terms of the incidence angle and the amplitude of the initial step, which can give rise to either subcritical or supercritical configurations, including the generalization to dispersive shock waves of the Mach reflection and expansion of viscous shocks and line solitons. An eightfold amplification of the amplitude of an obliquely incident flow upon a wall at the critical angle is demonstrated. Applications of the results include bore interactions in geophysical fluid dynamics.

DOI: 10.1103/cdvf-xnfw

The far-from-equilibrium, strongly nonlinear process of wave breaking is fundamental to the understanding of photonics [1–4], quantum superfluids [5–8], geophysics [9–12], and many other wave systems [13–16]. Whether referred to as an optical shock, a quantum shock, or an undular bore, wave breaking in these scenarios results in a dispersive shock wave (DSW). DSWs consist of a multiscale, unsteady, coherent collection of nonlinear waves that are distinctly different and inherently more complex than their more familiar viscous shock wave counterparts. While significant progress on experiments [2–4,11,13–16], modeling [17–19], and analysis [20,21] of one-dimensional (1D) DSWs has been achieved in recent years, the theory of multidimensional DSWs has been extremely limited [22–28].

The simplest generation mechanism for shock waves is a Riemann problem, which consists of step initial conditions (ICs) for the hydrodynamic variables [29–31]. In two spatial dimensions (2D), the Riemann problem consists of ICs that are piecewise constant in different sectors of the plane [32,33]. Such a scenario forms the foundation for the theoretical study of regular and Mach reflection or expansion in which an obliquely incident shock encounters a wall [34,35]. Mach reflection is a general nonlinear process that also applies to oblique soliton collisions. While there has been a great deal of study on the Mach reflection of viscous shocks and oblique solitons, there has been no study of this fundamental, multidimensional nonlinear wave process for DSWs.

In this Letter, we consider sectorial Riemann problems for the Kadomtsev-Petviashvili (KP) equation leading to the generation of two obliquely colliding DSWs, a problem that is related to the oblique interaction of a DSW with a wall. Numerical simulations of wedge-type ICs for different angles reveal a transition between two distinctive scenarios, which we identify as the bifurcation from Mach reflection or expansion (subcritical) to regular reflection or expansion (supercritical), respectively, of a DSW obliquely incident upon a wall. We analytically identify salient properties of the unsteady, 2D DSW patterns and their bifurcations including the critical angle, the leading-edge structure, the growth of the DSW Mach stem, and up to an eightfold amplification of the amplitude of the incident flow. Notably, patterns similar to our predictions have recently been observed in surface and internal water waves [36].

Kadomtsev-Petviashvili equation—The KP equation [44] is a prototypical universal model for weakly 2D, weakly nonlinear waves. It arises in a number of disparate physical settings such as shallow water [45,46], internal waves [47], plasmas [48], magnetic materials [49,50], cosmology [51–54], and Bose-Einstein condensates [55–57]. In rescaled and dimensionless variables, it can be written as

$$(u_t + uu_x + u_{xxx})_x + u_{yy} = 0. \tag{1}$$

The meaning of the variable u depends on the physical context considered, while x represents the main direction of propagation, y is a transverse spatial variable, and t is time. In shallow water, u quantifies the deviation of the water surface from its equilibrium value. The KP equation is also the prototypical infinite-dimensional completely integrable system in two spatial dimensions [58–60] with soliton solutions exhibiting resonance and web structure [61–64]. Importantly, even though Eq. (1) has been the subject of a large number of studies over the past 50 years, the temporal dynamics of solutions arising from generic ICs are still not well understood.

 © 2025 American Physical Society

For solutions that are independent of y, Eq. (1) reduces to the Korteweg–de Vries (KdV) equation $u_t + uu_x + u_{xxx} = 0$. In turn, the KdV equation is a dispersive regularization of the Hopf equation $u_t + uu_x = 0$. It is well known that increasing ICs for the Hopf equation give rise to rarefaction waves, while decreasing ICs give rise to shocks [65]. The dispersive regularization of the Hopf equation via the KdV equation for decreasing ICs gives rise instead to a DSW [20].

Line solitons and oblique DSWs—The KP equation (1) admits a three-parameter family of one-soliton solutions representing a solitary wave with amplitude a and slope q on a background $\bar{u}$, given by

$$u(x,y,t) = \bar{u} + a\mathrm{sech}^2\left(\sqrt{a/12}(x + qy - ct - x_o)\right), \quad (2)$$

where $q = \tan\phi$ quantifies the transverse inclination angle ϕ of the soliton and $c = C(a,q,\bar{u}) = \bar{u} + a/3 + q^2$ is the soliton propagation velocity along the x direction [66]. The solution is localized along $x + qy - ct = x_o$, which describes a (moving) line in the xy plane and is, therefore, referred to as a *line soliton*. The KP equation also admits an oblique version of the one-dimensional DSWs of the KdV equation [67], which we briefly describe since they play a key role in this Letter [36]. An oblique DSW of Eq. (1) consists of an expanding, highly oscillatory nonlinear wave train that is independent of the direction transverse to its propagation. It comprises two distinguished limits: the harmonic edge limit and the soliton edge limit. At the harmonic edge, which moves with the group velocity of linear waves for a particular wave vector, the wave amplitude vanishes. In contrast, at the soliton edge, which moves faster, with the phase velocity of a soliton (2) for a particular amplitude, the wave vector vanishes. The speed and properties of each limiting edge are completely determined by the initial jump height $\Delta = u_{\max} - u_{\min}$ and propagation slope q. For our purposes, the most important oblique DSW property is the soliton edge amplitude $a = a_s$, which is $a_s = 2\Delta$. These oblique DSWs will comprise the elemental building blocks that appear in the more complicated dynamical scenarios discussed next.

Wedge-shaped initial profiles—Below, we show that a variety of dynamical outcomes can arise from sectorial Riemann problems, and we classify and quantitatively characterize the resulting nonlinear phenomena. Specifically, we study the behavior of solutions of Eq. (1) arising from the class of step down ICs

$$u(x,y,0) = H\big(X(y) - x\big), \quad (3)$$

where $H(\xi)$ is the Heaviside step function and where, without loss of generality, we used the scaling and Galilean invariances of Eq. (1) [36,68] to set the step values to 1 for $x < X(y)$ and 0 for $x > X(y)$, implying $\Delta = 1$. The curve $x = X(y)$ describes the transition profile in the xy plane. If $X(y) = 0$ or $X(y)$ is constant, the solution of Eq. (1) is independent of y and, therefore, reduces to that of the KdV equation, whose behavior is well characterized [20,65,67]. Similarly, if $X(y) = q_o y$, with $q_o = \text{const}$, one can take advantage of the pseudo-rotation symmetry of the KP equation [36] to see that the resulting behavior is simply an oblique rarefaction wave (for an upward step) or an oblique DSW (downward step).

When the spatial profile of the step is a wedge, however, novel 2D wave structures arise. We take $X(y)$ to be a smooth version of the wedge profile $X(y) = -q_o|y|$, with $q_o = \text{const}$. We then consider the following types of wedge ICs: (I) downward step with an acute angle ($q_o > 0$) and (II) downward step with an obtuse angle ($q_o < 0$). As we show next, these ICs lead to wave breaking and the generation of multidimensional DSWs. One could also consider two additional wedge types: (III) upward step with an acute angle and (IV) upward step with an obtuse angle. The time evolution of wedge types III and IV produces 2D rarefaction waves.

Since Eqs. (1) and (3) are invariant under $y \mapsto -y$, all solutions satisfy $u(x,y,t) = u(x,-y,t)$. Thus, $u_y(x,0,t) = 0$, which is the slip wall boundary condition at $y = 0$ for inviscid water or internal wave theory [69]. Consequently, by this nonlinear analog of the method of images, solutions constrained to $y > 0$ correspond to an oblique step in amplitude incident with a wall at $y = 0$ and the subsequent reflection ($q_o < 0$) or expansion ($q_o > 0$) of the flow, analogous to the case of Mach reflection [70] and expansion [71] of an oblique soliton upon a wall. (Such scenarios could occur during the flood or ebb tide of the ocean, respectively.)

Temporal dynamics and its classification—The dynamics produced by wedge types I and II are illustrated in Figs. 1–3 [36], which demonstrate that the time evolution gives rise to a rich variety of nonlinear phenomena, including the emergence of curved DSW fronts, Mach stems, and multiphase regions with curved boundaries, all of which are due to fundamental nonlinear processes.

When $q_o > 0$, the two oblique DSWs propagate away from each other, resulting in an expansive configuration. Conversely, when $q_o < 0$, they propagate toward each other, resulting in a compressive configuration. In all cases, the time evolution results in the formation of two oblique DSWs for large values of $|y|$ (more clearly visible in the earlier time snapshots), which is accurately described by modulation oscillations [36]. The leading edge of both DSWs is an oblique line soliton with slope $\pm q_o$ and amplitude $a_s = 2$, equaling twice the size of the initial jump, as in the 1D case.

The crucial differences in dynamical outcomes lie in the nature of the nonlinear interactions between these two oblique DSWs, which determine the behavior of the solution near $y = 0$. For ease of presentation, we next

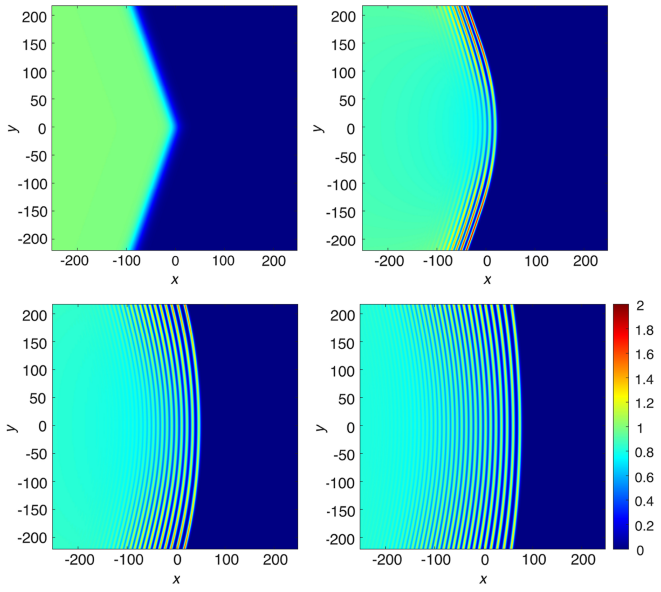

FIG. 1. Solution of the KP equation produced by a subcritical type I wedge with $q_o = 0.4$ at times $t = 0$, 75, 150, and 225. Note the formation of a vertical DSW in the portion of the domain near the x axis.

introduce terminology that will be fully justified in a later portion of the Letter. Specifically, we will show that, for both types I and II wedges, the threshold $q_{\rm cr} = \sqrt{2}$ discriminates between different dynamical outcomes. Accordingly, *we refer to wedges with* $0 < |q_o| < q_{\rm cr}$ *as*

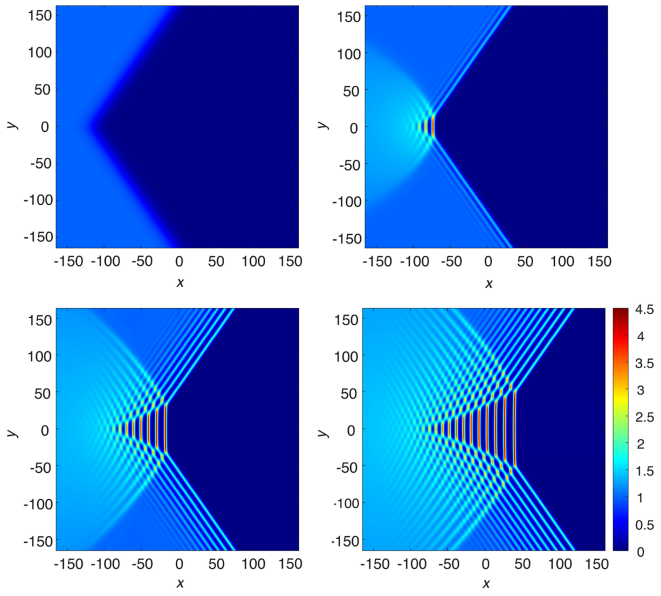

FIG. 2. Solution of the KP equation produced by a subcritical type II wedge with $q_o = -0.7$ at times $t = 0$, 40, 80, and 120. Note the formation of a vertical DSW with high amplitude near the x axis as well as the presence of two expanding regions, symmetrically located with respect to the x axis, characterized by multiphase oscillations.

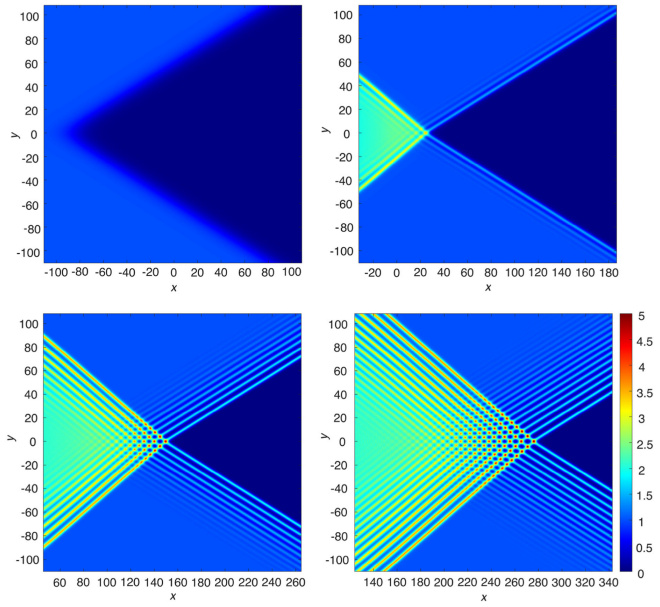

FIG. 3. The same as Fig. 2 but for a supercritical type II wedge with $q_o = -1.6$. Note the formation of a single expanding region of multiphase oscillations around the x axis as well as the higher propagation speed along the x direction compared to Fig. 2.

subcritical and to wedges with $|q_o| > q_{\rm cr}$ *as supercritical.* For a generic initial jump with $u_- > u_+$, the scaling invariance of the KP equation can be used to show that the corresponding critical slope is $q_{\rm cr} = \sqrt{2\Delta}$.

For subcritical type I wedges (Fig. 1), the time evolution eventually produces a region characterized by an expanding, vertical DSW, which smoothly connects the two far-field oblique DSWs via a curved front and is a generalization to DSWs of the Mach expansion of oblique line solitons [36,71]. In contrast, no vertical DSW is produced by supercritical type I wedges (cf. Fig. S1 in [36]), and in this case the amplitude of the DSW around $y = 0$ decays in time, while its spatial profile tends to a parabolic shape (see below and [36]).

The dynamics produced by type II wedges (shown in Figs. 2 and 3) are even richer, and the qualitative difference between subcritical and supercritical type II wedges is evident upon comparing Figs. 2 and 3. For subcritical type II wedges (Fig. 2), the interaction between the two oblique DSWs produces an expanding region around $y = 0$ characterized by a third, vertical DSW. This phenomenon is a generalization to DSWs of the Mach stem produced by the oblique interaction of two line solitons [34,36,61,63,72] or the Mach reflection of viscous shock waves [35,73,74]. Accordingly, we refer to the vertical DSW in subcritical type I and II wedges as the *stem DSW*. In contrast, for supercritical wedges (Fig. 3), no stem DSW is produced. On the other hand, for both subcritical and supercritical type II wedges, the interaction between these oblique DSWs produces expanding regions characterized by modulated multiphase oscillations [36]. Specifically, for

subcritical type II wedges (Fig. 2 and [36]), two such regions are produced, symmetrically located above and below $y = 0$. In contrast, for supercritical type II wedges (Fig. 3 and [36]), a single such region is produced around the x axis.

Quantitative analysis—As we show next, both subcritical and supercritical wedges can be characterized quantitatively. In particular, the difference between subcritical and supercritical wedges can be understood by looking at the interaction between the leading-edge solitons of the oblique DSWs. The reason for this is twofold: first, because the soliton edge is the largest and, therefore, most prominent feature of the DSW and, second, because interactions between KPII line solitons have been well studied and characterized [61–64,75–78]. Accordingly, we look at the interaction between oblique solitons with amplitude $a_s = 2$ (the amplitude of the leading edge soliton for the two oblique DSWs) and slopes $\pm q_o$. Then, using the results of [63,70,71], one sees that the threshold $q_{\rm cr} = \sqrt{2}$ between subcritical and supercritical wedges is precisely the threshold between ordinary and resonant two-soliton interactions [36].

For subcritical type II wedges, both the amplitude and the expansion rate of the vertical soliton at the leading edge of the stem DSW can be captured using the analysis of oblique soliton interactions in [70,71]. Specifically, the leading-edge soliton in the stem DSW is located in the region $|y| \le V_o t$, where the vertical expansion rate $V_o(a, q)$ is [71]

$$V_o(a, q) = 2(\sqrt{a} + q)/3. \tag{4}$$

Here $q = q_o$, and $a = a_s = 2$. This prediction is in excellent agreement with the numerical results for all $-q_{\rm cr} < q_o < 0$ [36]. Note from Fig. 2 that the amplitude A_o of the leading-edge soliton stem DSW in subcritical type II wedges is much larger than that of the leading-edge solitons in the oblique DSWs. The prediction for the amplitude of the Mach stem for an oblique soliton interaction [Eq. (5.3a) in [70]] yields immediately

$$A_o(a, q) = (\sqrt{a} - q)^2 \tag{5}$$

(again with $q = q_o$ and $a = a_s$). As shown in Fig. 4 (left), Eq. (5) is in excellent agreement with the results of numerical simulations for all $-q_{\rm cr} < q_o < 0$. The largest solution amplitude is produced when $q_o = -\sqrt{a_s}$, which yields $A_{\rm max} = 4a_s$, the well-known fourfold amplification of an oblique soliton incident upon a wall. Since $a_s = 2\Delta$ for the oblique DSW, however, the scaling symmetry of Eq. (1) [36] implies that the maximum amplitude for an arbitrary jump of size Δ is $A_{\rm max} = 8\Delta$, i.e., an eightfold increase in the amplitude. Finally, as shown in Fig. 4 (right), the numerically computed horizontal soliton speed dx/dt of the leading-edge soliton in the stem DSW also

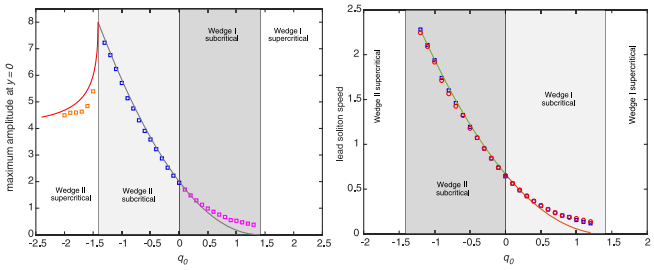

FIG. 4. Left: numerically computed amplitude (blue and magenta squares) of the leading-edge soliton in the stem DSW for subcritical type I and II wedges as a function of q_o; maximum amplitude for supercritical type II wedges (orange squares) and theoretical predictions from Eqs. (5) and (6). Right: numerically computed horizontal propagation speed dx/dt for subcritical type I and II wedges (squares), together with the theoretical prediction $C(A_o, 0, 0)$ (solid curve) and the speed corresponding to the measured soliton amplitude (circles).

agrees very well with the soliton amplitude-speed relation $C(a, q, \bar{u})$ with $a = A_o$ and $\bar{u} = q = 0$.

In supercritical type II wedges, the maximum amplitude at $y = 0$ is approximately given by the maximum of the two-soliton solution associated with two solitons with amplitude $a = a_s$ and slope $q = \pm q_o$ [64], which is found to be [36]

$$u_{\rm max}(q) = -2q\left(\sqrt{\sqrt{2}q + 2}\sqrt{2\sqrt{2}q - 4} - 2q\right). \tag{6}$$

This prediction agrees fairly well with the results of numerical simulations for $q_o < -q_{\rm cr}$ [see Fig. 4 (left)], and it also limits to the maximum value of 8Δ as q_o tends to $-q_{\rm cr}$.

The amplitude of the leading-edge soliton in the stem DSW in subcritical type I wedges also agrees with the theoretical prediction from Eq. (5); see Fig. 4 (left) (with small discrepancies when q_o is close to $q_{\rm cr}$, likely due to the fact that measuring small amplitudes is more sensitive to small numerical errors due to dispersive radiation). Moreover, as shown in Fig. 4 (right), the horizontal speed of the lead soliton in the stem DSW compares well with the predicted speed $C(A_o, 0, 0)$ (again with small discrepancies for $q_o \sim q_{\rm cr}$). Finally, for all $0 < q_o < q_{\rm cr}$, the measured amplitude and speed of the lead soliton agrees well with the soliton amplitude-speed relation given by $C(a, 0, 0)$.

In supercritical type I wedges, the solution near $y = 0$ tends to a DSW of the cylindrical KdV (cKdV) reduction of the KP equation, whose amplitude decays in time. In particular, by extracting the shape of the DSW near $y = 0$, fitting it to a parabolic profile, and extracting via a linear regression the time dependence of the parabolic curvature coefficient $p(t) = p_o t + p_1$, one can quantify how well a DSW approaches that of the cKdV equation [36]. For supercritical type I wedges, the numerically obtained time-dependence coefficient p_o reaches a steady

value that agrees well with the predicted value of 4 for the cKdV reduction [36]. Conversely, for subcritical type I wedges, the temporal dependence of the parabolic front is superlinear (i.e., the numerically computed coefficient p_o is itself an increasing function of time) [36], consistent with the fact that the solution near $y = 0$ tends to a constant-amplitude stem DSW.

Discussion—The results of this Letter are robust with respect to numerical perturbations and can, therefore, be expected to be observable in nature. The dynamics of subcritical and supercritical type II wedges appears to reproduce phenomena recently observed in the Qiantang river tide [36]. In particular, a new type of "matrix tide," observed in 2024, depicts the oblique collision of two undular bores and a corresponding interference pattern that is very similar to that of the supercritical type II wedge case in Fig. 3. Also, the dynamics of type I wedges are common in near-shore internal wave dynamics and in rivers subject to tide-generated undular bores [36]. Applications for expansive ICs include the generation of parabolic DSWs from high-speed ferries in shallow water and atmospheric lee waves from mountains [79–82]. Conversely, compressive conditions model a flood-tide-generated undular bore obliquely impinging upon an obstacle, e.g., a sill, resulting in a Mach stem DSW (subcritical case) or a multiphase DSW (supercritical case) [83]. We also expect that similar phenomena will arise in other related physical models, including the 2D-Benjamin-Ono equation, which governs the evolution of weakly 2D internal waves, where curved DSWs similar to those in Fig. 1 are observed [36].

Avenues for future study include a characterization of the results via the (KPWS), namely. the Whitham modulation equations for the KP equation [68]. This, however, is a nontrivial task [36]. Another direction will be a study of the quantitative behavior of types III and IV wedges and, in particular, the question of whether there is also a critical angle in that case. Finally, an important goal will be the experimental realization of these phenomena in shallow and internal gravity water wave tanks.

Acknowledgments—We thank the Isaac Newton Institute for Mathematical Sciences for support and hospitality during the program "Dispersive Hydrodynamics" (Engineering and Physical Sciences Research Council Grant No. EP/R014604/1). We also thank Yifeng Mao for help with sources for the Qiantang river bore observations. This work was partially supported by the National Science Foundation under Grants No. DMS-2009487 (G. B.) and No. DMS-2306319 (M. A. H.).

[1] W. Wan, S. Jia, and J. W. Fleischer, Nat. Phys. **3**, 46 (2007).
[2] G. Xu, M. Conforti, A. Kudlinski, A. Mussot, and S. Trillo, Phys. Rev. Lett. **118**, 254101 (2017).
[3] T. Bienaimé, M. Isoard, Q. Fontaine, A. Bramati, A. M. Kamchatnov, Q. Glorieux, and N. Pavloff, Phys. Rev. Lett. **126**, 183901 (2021).
[4] A. Bendahmane, G. Xu, M. Conforti, A. Kudlinski, A. Mussot, and S. Trillo, Nat. Commun. **13**, 3137 (2022).
[5] Z. Dutton, M. Budde, C. Slowe, and L. V. Hau, Science **293**, 663 (2001).
[6] M. A. Hoefer, M. J. Ablowitz, I. Coddington, E. A. Cornell, P. Engels, and V. Schweikhard, Phys. Rev. A **74**, 023623 (2006).
[7] J. A. Joseph, J. E. Thomas, M. Kulkarni, and A. G. Abanov, Phys. Rev. Lett. **106**, 150401 (2011).
[8] M. E. Mossman, M. A. Hoefer, K. Julien, P. G. Kevrekidis, and P. Engels, Nat. Commun. **9**, 4665 (2018).
[9] J. D. Nash and J. N. Moum, Nature (London) **437**, 400 (2005).
[10] A. Scotti, R. C. Beardsley, and B. Butman, J. Geophys. Res. **112**, C10001 (2007).
[11] S. Trillo, G. Deng, G. Biondini, M. Klein, G. F. Clauss, A. Chabchoub, and M. Onorato, Phys. Rev. Lett. **117**, 144102 (2016).
[12] L. Li, R. Pawlowicz, and C. Wang, J. Geophys. Res. **123**, 5706 (2018).
[13] Y. C. Mo, R. A. Kishek, D. Feldman, I. Haber, B. Beaudoin, P. G. O'Shea, and J. C. T. Thangaraj, Phys. Rev. Lett. **110**, 084802 (2013).
[14] M. D. Maiden, N. K. Lowman, D. V. Anderson, M. E. Schubert, and M. A. Hoefer, Phys. Rev. Lett. **116**, 174501 (2016).
[15] P. A. Praveen Janantha, P. Sprenger, M. A. Hoefer, and M. Wu, Phys. Rev. Lett. **119**, 024101 (2017).
[16] J. Li, S. Chockalingam, and T. Cohen, Phys. Rev. Lett. **127**, 014302 (2021).
[17] S. Trillo, M. Klein, G. Clauss, and M. Onorato, Physica (Amsterdam) **333D**, 276 (2016).
[18] R. Chassagne, A. G. Filippini, M. Ricchiuto, and P. Bonneton, J. Fluid Mech. **870**, 595 (2019).
[19] S. A. Simmons, F. A. Bayocboc, J. C. Pillay, D. Colas, I. P. McCulloch, and K. V. Kheruntsyan, Phys. Rev. Lett. **125**, 180401 (2020).
[20] G. El and M. A. Hoefer, Physica (Amsterdam) **333D**, 11 (2016).
[21] P. D. Miller, Physica (Amsterdam) **333D**, 66 (2016).
[22] M. J. Ablowitz, A. Demirci, and Y.-P. Ma, Physica (Amsterdam) **333D**, 84 (2016).
[23] A. V. Gurevich, A. L. Krylov, V. V. Khodorovskii, and G. A. El, Sov. Phys. JETP **81**, 87 (1995).
[24] A. V. Gurevich, A. L. Krylov, V. V. Khodorovskii, and G. A. El, Sov. Phys. JETP **82**, 709 (1996).
[25] G. A. El, A. M. Kamchatnov, V. V. Khodorovskii, E. S. Annibale, and A. Gammal, Phys. Rev. E **80**, 046317 (2009).
[26] M. A. Hoefer and B. Ilan, SIAM Multiscale Model. Simul. **10**, 306 (2012).
[27] M. A. Hoefer, G. A. El, and A. M. Kamchatnov, SIAM J. Appl. Math. **77**, 1352 (2017).
[28] T. Grava, C. Klein, and G. Pitton, Proc. R. Soc. A **474**, 20170458 (2018).
[29] P. D. Lax, *Hyperbolic Systems of Conservation Laws and the Mathematical Theory of Shock Waves* (SIAM, Philadelphia, 1973).

[30] R. Courant and K. O. Friedrichs, *Supersonic Flow and Shock Waves* (Springer, New York, 1976).
[31] R. Courant and H. Hilbert, *Methods of Mathematical Physics* (Interscience, New York, 1962).
[32] T. Zhang and Y. X. Zheng, SIAM J. Math. Anal. **21**, 593 (1990).
[33] A. Kurganov and E. Tadmor, Numer. Methods Partial Differ. Equ. **18**, 584 (2002).
[34] J. W. Miles, J. Fluid Mech. **79**, 171 (1977).
[35] M. Brio and J. K. Hunter, Physica (Amsterdam) **60D**, 194 (1992).
[36] See Supplemental Material at http://link.aps.org/supplemental/10.1103/cdvf-xnfw for further details, including Refs. [37–43].
[37] F. W. Olver, D. W. Lozier, R. F. Boisvert, and C. W. Clark, *NIST Handbook of Mathematical Functions* (Cambridge University Press, Cambridge, England, 2010).
[38] H. Segur and A. Finkel, Stud. Appl. Math. **73**, 183 (1985).
[39] T. Grava and F. Tian, Commun. Pure Appl. Math. **55**, 1569 (2002).
[40] T. Bonnemain, G. Biondini, B. Doyon, G. Roberti, and G. A. El, Phys. Rev. Res. **7**, 013143 (2025).
[41] Y. Zheng, *Systems of Conservation Laws: Two-Dimensional Riemann Problems* (Springer, New York, 2001).
[42] I. M. Krichever, Funct. Anal. Appl. **22**, 37 (1988).
[43] M. A. Hoefer and M. J. Ablowitz, Physica (Amsterdam) **236D**, 44 (2007).
[44] B. B. Kadomtsev and V. I. Petviashvili, Sov. Phys. Dokl. **15**, 539 (1970).
[45] M. J. Ablowitz and H. Segur, *Solitons and the Inverse Scattering Transform* (SIAM, Philadelphia, 1981).
[46] Y. Kodama, *Solitons in Two-Dimensional Shallow Water* (SIAM, Philadelphia, 2018).
[47] M. J. Ablowitz and H. Segur, J. Fluid Mech. **92**, 691 (1979).
[48] E. Infeld and G. Rowlands, *Nonlinear Waves, Solitons and Chaos* (Cambridge University Press, Cambridge, England, 2000).
[49] E. G. Fal'kovich and S. K. Turitsyn, Sov. Phys. JETP **62**, 146 (1985).
[50] H. Leblond, J. Phys. A **35**, 10149 (2002).
[51] R. Kates, Astron. Astrophys. **194**, 3 (1988).
[52] S. I. Vacaru and D. Singleton, Classical Quantum Gravity **19**, 2793 (2002).
[53] I. Melnikov, D. Mihalache, and N. Panoiu, Opt. Commun. **181**, 345 (2000).
[54] D. Duncan, J. Eilbeck, C. Walshaw, and V. Zakharov, Phys. Lett. A **158**, 107 (1991).
[55] H. Guo-Xiang and Z. Shan-Hua, Chin. Phys. Lett. **19**, 17 (2002).
[56] N. G. Berloff, Phys. Rev. B **65**, 174518 (2002).
[57] N. G. Berloff, Phys. Rev. A **69**, 053601 (2004).
[58] S. P. Novikov, S. V. Manakov, L. P. Pitaevskii, and V. E. Zakharov, *Theory of Solitons: The Inverse Scattering Transform* (Plenum, New York, 1984).
[59] M. J. Ablowitz and P. A. Clarkson, *Solitons, Nonlinear Evolution Equations and Inverse Scattering* (Cambridge University Press, Cambridge, England, 1991).
[60] B. G. Konopelchenko, *Solitons in Multidimensions: Inverse Spectral Transform Method* (World Scientific, Singapore, 1993).
[61] G. Biondini and Y. Kodama, J. Phys. A **36**, 10519 (2003).
[62] G. Biondini and S. Chakravarty, J. Math. Phys. (N.Y.) **47**, 033514 (2006).
[63] G. Biondini, Phys. Rev. Lett. **99**, 064103 (2007).
[64] Y. Kodama, *KP Solitons and the Grassmannians: Combinatorics and Geometry of Two-Dimensional Wave Patterns* (Springer, New York, 2017).
[65] G. B. Whitham, *Linear and Nonlinear Waves* (Wiley, New York, 1974).
[66] S. Ryskamp, M. A. Hoefer, and G. Biondini, Nonlinearity **34**, 3583 (2021).
[67] A. V. Gurevich and L. P. Pitaevskii, Zh. Eksp. Teor. Fiz. **65**, 590 (1974).
[68] M. J. Ablowitz, G. Biondini, and Q. Wang, Proc. R. Soc. A **473**, 20160695 (2017).
[69] P. G. Baines, *Topographic Effects in Stratified Flows* (Cambridge University Press, Cambridge, England, 1998).
[70] S. Ryskamp, M. A. Hoefer, and G. Biondini, Proc. R. Soc. A **478**, 20210823 (2022).
[71] S. Ryskamp, M. Maiden, M. A. Hoefer, and G. Biondini, J. Fluid Mech. **909**, A24 (2021).
[72] W. Li, H. Yeh, and Y. Kodama, J. Fluid Mech. **672**, 326 (2011).
[73] E. Mach and J. Wosyka, Sitzungsber. Akad. Wiss. Wien Math. Naturwiss. Kl. Abt. 1 **72**, 44 (1875).
[74] P. Krehl and M. van der Geest, Shock Waves **1**, 3 (1991).
[75] J. Satsuma, J. Phys. Soc. Jpn. **40**, 286 (1976).
[76] N. Yajima, M. Oikawa, and S. Satsuma, J. Phys. Soc. Jpn. **44**, 1711 (1978).
[77] F. Kako and N. Yajima, J. Phys. Soc. Jpn. **49**, 2063 (1980).
[78] F. Kako and N. Yajima, J. Phys. Soc. Jpn. **51**, 11 (1982).
[79] S.-J. Lee and R. H. J. Grimshaw, Phys. Fluids A **2**, 194 (1990).
[80] Y. Li and P. D. Sclavounos, J. Fluid Mech. **470**, 383 (2002).
[81] T. Soomere, Appl. Mech. Rev. **60**, 120 (2007).
[82] A. Mann, Proc. Natl. Acad. Sci. U.S.A. **116**, 19218 (2019).
[83] C. Yuan and Z. Wang, J. Fluid Mech. **936**, A20 (2022).
[84] C. Klein, C. Sparber, and P. Markowich, J. Nonlinear Sci. **17**, 429 (2007).
[85] A. Liu and T. Trogdon, Applied Numerical Mathematics **192**, 19 (2023).

End Matter

Evolutionary form of the KP equation—The ICs for the KP equation (1) must satisfy a "constant-mass" constraint, which is obtained by integrating Eq. (1) in x over the whole real axis, to obtain, for solutions that are bounded in y, the constraint

$$\frac{\partial}{\partial y}\int_{\mathbb{R}} u(x,y,t)\mathrm{d}x = 0. \tag{A1}$$

In the numerical simulations, we enforce this constraint by ensuring that the integral of the IC with respect to x is independent of y (see below for details).

The KP equation (1) can also be written in evolutionary form as

$$u_t + uu_x + u_{xxx} + \partial_x^{-1} u_{yy} = 0, \tag{A2}$$

where the antiderivative ∂_x^{-1}, defined by

$$\partial_x^{-1} f(x) = \frac{1}{2}\left(\int_{-\infty}^{x} f(\xi)\mathrm{d}\xi - \int_{x}^{\infty} f(\xi)\mathrm{d}\xi\right), \tag{A3}$$

can also be understood as the operator whose Fourier multiplier is the singular symbol $-i/k$, as is done in the numerical method used to integrate Eq. (1), which is discussed next.

Physical scales for shallow water waves—In shallow water, when the undisturbed water depth h is small relative to the typical wavelength and the maximum wave amplitude $a_{\max}$ is small compared to h, for weakly two-dimensional waves, one obtains the KP equation in dimensional form as [45,48]

$$\frac{1}{\sqrt{gh}} u_{XT} + u_{XX} + \frac{3}{2h}(uu_X)_X + \frac{h^2}{6}\left(1 - \frac{3\tau}{\rho g h^2}\right) u_{XXXX} = -\frac{1}{2} u_{YY}, \tag{A4}$$

where X, Y, and T are dimensional spatial and temporal variables, g is the usual gravity acceleration, ρ is the uniform density of the fluid, and τ is the surface tension of the fluid. Equation (A4) is converted to the dimensionless form in Eq. (1) by letting $x = \sqrt{\epsilon} X/h$, $y = \epsilon Y/h$, and $t = T\sqrt{\epsilon g/h}$, where $\epsilon = a_{\max}/h \ll 1$. We assume $\rho g h > 3\tau$ in Eq. (1).

Whitham equations for the KdV equation—The Whitham modulation equations for the KdV equation describe spatiotemporal modulations of its periodic solutions and in diagonal form are given by $\partial r_j/\partial t + V_j \partial r_j/\partial x = 0$, where r_1, r_2, and r_3 are the Riemann invariants and the characteristic speeds V_1, V_2, and V_3 are given explicitly in terms of r_1, r_2, and r_3. [65]. In [67], Gurevich and Pitaevskii showed that the DSW generated by a downward step from $u_{\max}$ to $u_{\min}$ is accurately described by a self-similar solution of the Whitham equations, which is easily generalized to slanted DSWs of the KP equation as follows: $r_1(x,y,t) \equiv u_{\min}$, $r_3(x,y,t) \equiv u_{\max}$, and $r_2(x,y,t) = R_2(\xi)$ with $\xi = (x+qy)/t$, where $R_2(\xi) = u_{\min}$ for $\xi < \xi_{\min}$ and $R_2(\xi) = u_{\max}$ for $\xi > \xi_{\max}$, with $\xi_{\min} = -\Delta + u_{\min}$, $\xi_{\max} = \frac{2}{3}\Delta + u_{\min}$, and $\Delta = (u_{\max} - u_{\min})$. For $\xi_{\min} < \xi < \xi_{\max}$, $R_2(\xi)$ is given by inverting the above expression for m as a function of r_1, r_2, and r_3, i.e., $R_2 = r_1 + m\Delta$, with $\xi = V_2(m)$, where $V_2(m) = u_{\max} + \frac{1}{3}\Delta\{1 + m + 2m(1-m)K(m)/[E(m) - (1-m)K(m)]\}$ and $E(m)$ is the complete elliptic integral of the second kind.

Numerical integration algorithm—The nonlinearity, nonlocality, and stiff fourth derivative term in Eq. (1) make it challenging to simulate numerically. To overcome these challenges, we use a fourth-order integrating factor Runge-Kutta (IFRK4) method, as in [84]. The method treats the nonlocal and stiff portions of the evolution equation with spectral accuracy and the nonlinear portion of the equation with fourth-order accuracy, as described next. Introduce the 2D Fourier transform xpair as

$$\hat{f}(k,l) = \mathscr{F}[f(x,y)] = \iint_{\mathbb{R}^2} e^{-i(kx+ly)} f(x,y)\mathrm{d}x\mathrm{d}y, \tag{A5a}$$

$$f(x,y) = \mathscr{F}^{-1}[\hat{f}(k,l)] = \frac{1}{2\pi}\iint_{\mathbb{R}^2} e^{i(kx+ly)} F(k,l)\mathrm{d}k\mathrm{d}l. \tag{A5b}$$

Taking the Fourier transform of Eq. (1) yields

$$k\hat{u}_t = i(k^4 - \sigma l^2)\hat{u} - k\mathscr{F}[uu_x]. \tag{A6}$$

It is then convenient to introduce the new dependent variable

$$\hat{v}(k,l,t) := e^{-i(k^3 - \sigma l^2/k)t}\hat{u}(k,l,t), \tag{A7}$$

which solves the linear part of Eq. (A6). Once $\hat{v}$ is known, one can calculate u by inverting Eq. (A7), namely,

$$u(x,y,t) = \mathscr{F}^{-1}[e^{i(k^3 - \sigma l^2/k)t}\hat{v}(k,l,t)]. \tag{A8}$$

Moreover, substituting Eq. (A7) into Eq. (A6) yields

$$\hat{v}_t = -(ik/2)e^{-i(k^3 - \sigma l^2/k)t}\mathscr{F}[u^2], \tag{A9}$$

(note $\mathscr{F}[uu_x] = \frac{1}{2}ik\mathscr{F}[u^2]$), which is an ordinary differential equation without stiff terms and which can, therefore, be efficiently solved with RK4. After setting $\hat{v}(k,l,0) = \hat{u}(k,l,0)$, the evaluation of the right-hand side of Eq. (A9) at each time step can be done via the following steps: (a) Use Eq. (A7) to get $\hat{u}(k,l,t)$ from $\hat{v}(k,l,t)$ at the current time step. (b) Take the inverse fast Fourier transform (IFFT) of $\hat{u}(k,l,t)$ to get $u(x,y,t)$. (c) Finally, take the FFT of the term u^2. At regularly spaced time intervals, one then uses Eq. (A8) to save a snapshot of the solution of the KP equation (1).

Numerical zero-mass constraint—The implementation of the above IFRK4 algorithm requires an additional constraint because of the exponential factor $\exp[i(k^3 - \sigma l^2/k)t]$ appearing in Eqs. (A7) and (A8). The division by k is singular for all $k = 0$ modes when $l \neq 0$. However, Eq. (A6) shows that no singularity arises if $\hat{u}(0, l, t) = 0$. The definition (A5a) of the Fourier transform implies that the condition $\hat{u}(0, l, t) = 0$ corresponds to the zero-mass condition $\int_{\mathbb{R}} u(x, y, t)\mathrm{d}x = 0$ for all $y \in \mathbb{R}$. That is, the total mass of the solution integrated along the x direction should be zero for all $y \in \mathbb{R}$. Note that, if the zero-mass constraint is satisfied for all $y \in \mathbb{R}$, Eq. (A1) is also satisfied. Note also that, when both $k = 0$ and $l = 0$, Eq. (A6) is trivially satisfied. On the other hand, if the zero-mass constraint is satisfied for all $y \in \mathbb{R}$, one has that $\hat{u}(0, 0, t) = \iint_{\mathbb{R}^2} u(x, y, t)\mathrm{d}x\mathrm{d}y = 0$ for all t.

We deal with this constraint by manually setting $\hat{u}(0, l, t) = 0$ at each time step for all $l \neq 0$ and by setting $\hat{u}(0, 0, t) = \hat{u}(0, 0, 0)$ for all t. The latter constraint can be satisfied without loss of generality by using the Galilean invariance of the KP equation, namely, the fact that an overall upward or downward shift of $u(x, y, t)$ simply amounts to a constant shift in the velocity of the solution.

Combined spatial domain: In order to use Fourier methods, the IC must be periodic in x and y. To deal with this constraint, it is convenient to combine all four wedge types into a single IC on an enlarged spatial domain, as shown in Fig. 5. Rather than evolving each of the four wedge types separately, we therefore run a single simulation on the enlarged domain. The time evolution of each individual wedge is recovered by simply selecting a different portion of this larger domain (cf. Fig. 5). The size of the enlarged spatial domain must be large enough so that effects from one wedge do not leak into any other subdomain during the time ranges considered.

Numerical IC implementation—A sharp step discontinuity corresponds to choosing the IC in Eq. (1) as $u(x,y,0) = H(x - x_1 + q_o|y|) - H(x - x_2 + q_o|y|)$, where $H(x)$ is the Heaviside step function. The quantities x_1 and x_2 vary the width and placement of the plateau and q_o its slope in the xy plane. The width of the plateau is simply $x_2 - x_1$. Since the Heaviside function and absolute value function in y are not smooth, however, this choice has the effect of exciting high-wave-number modes that can spoil the accuracy and even produce numerical instabilities. Therefore, to minimize high-wave-number components it is convenient to replace both $H(x)$ and $|y|$ with suitable smooth functions. Namely, we smooth out the transition between the values 0 and 1 along the x direction by replacing $H(\xi)$ with

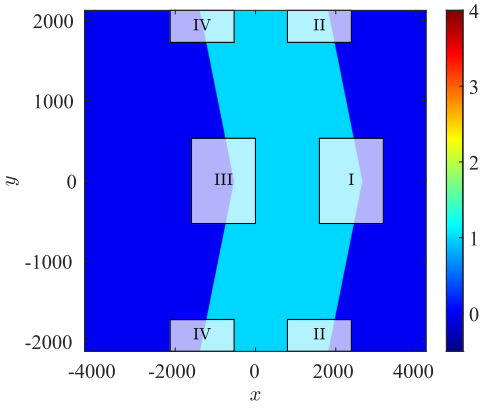

FIG. 5. The four wedge-type ICs combined on a single, enlarged physical domain. Here, $|q_o| = 0.4$.

$$H_\delta(\xi) = [1 + \tanh(\xi/\delta)]/2, \tag{A10}$$

where the parameter δ quantifies the steepness of the transition. The actual Heaviside function is recovered in the limit $\delta \to 0^+$. Similarly, the corner at $y = 0$ produced the absolute value function $|y|$ in the ICs is smoothed out by replacing it with $A(y)$, where $A'(y) = \tanh(ay)$ with a steepness parameter a, so that

$$A(y) = \int_0^y \tanh(ay)\mathrm{d}y = (1/a)\log[\cosh(ay)].$$

Since the numerical algorithm uses periodic boundary conditions (BCs), however, the corner of the IC at $y = \pm y_{\max}$ must also be smoothed out. This is accomplished by letting

$$A'(y) = \tanh(ay) - \tanh[a(y + y_{\max})] + \tanh[a(y - y_{\max})], \tag{A11}$$

so that $A'(y)$ is also continuous at $y = \pm y_{\max}$ and where we used that $y_{\min} = -y_{\max}$. Accordingly, we take

$$A(y) = (1/a)[\log[\cosh(ay)] - \log\{\cosh[a(y + y_{\max})]\} - \log\{\cosh[a(y - y_{\max})]\} + 2\log[\cosh(ay_{\max})]]. \tag{A12}$$

The evaluation of $A(y)$ also requires care, because the spatial domains are very large. The solution to this problem is use the fact that, for all $z \in \mathbb{R}$, $\log(\cosh z) = |z| - \log 2 + \log(1 + e^{-2|z|})$. The numerical implementation of $A(y)$ then uses Eq. (A12) with all the log cosh functions evaluated as described above. Summarizing, we implement the steplike wedge IC types I–IV on the combined spatial domain as

$$u(x, y, 0) = H_\delta[x - x_1 + q_o A(y)] - H_\delta[x - x_2 + q_o A(y)], \tag{A13}$$

with $H_\delta(x)$ and $A(y)$ as above.

Artificial damping—The above wedge ICs result in the production of trailing dispersive waves. Since the IFRK4

algorithm employs periodic BCs, we want to prevent these phenomena from reaching the domain boundary and subsequently corrupting the nonlinear phenomena on the other side.

An efficient solution to this issue is to use artificial damping, generalizing the approach of [85] to two spatial dimensions by adding the term $\alpha\sigma(x)(u_{xx}+u_{yy})$ to the right-hand side of Eq. (A2), where the function $\sigma(x)$ defines the region in which damping will take place and α quantifies the amount of damping applied. This term attenuates the trailing phenomena over the unused portion of the computational domain. Specifically, we take $\sigma(x)=1-\{\tanh[(x-x_3)/\delta]-\tanh[(x-x_4)]/\delta\}/2$, with δ as above and x_3 and x_4 chosen so that the region of the spatial domain in which the DSWs are contained is not damped.

Because of the stiffness of the dissipative terms, to evolve Eq. (1) with the artificial damping term added, we use an alternating direction Crank-Nicolson implicit method. At each time step, the numerical solver performs the following steps: (i) Evolve the system according to the KP equation, as described above. (ii) Evolve the system according to the damping term in the x direction over the same time. (iii) Evolve the damped portion of the domain over the same time step subject to damping in the y direction. The use of the alternating direction scheme allows one to use tridiagonal matrices in the Crank-Nicolson scheme. The resulting linear systems of equations are solved with a least-squares solver. The inclusion of this solver roughly triples the run-time. However, the artificial damping is effective enough at curtailing the dispersive phenomena that the overall size of the computational domain (and with it the number of grid points) can be decreased, resulting in a decrease in the overall simulation time for a given desired accuracy.

Integration parameters: The computational domain must be large enough to accurately capture the long-time behavior. We chose $x_{\mathrm{xmax}}=5000$ and $x_{\mathrm{xmin}}=-x_{\mathrm{max}}$. We also chose $y_{\mathrm{min}}=-y_{\mathrm{max}}$, with $y_{\mathrm{max}}=1250$. The number of Fourier modes must be taken to be correspondingly large in order to maintain spatial accuracy. We choose the number of Fourier modes along the x direction and the y direction to be, respectively, 2^{15} and 2^{13}. Finally, we chose a time integration step size of $\Delta t=10^{-2}$, which was sufficient to ensure the accuracy of all numerical results reported.